

See discussions, stats, and author profiles for this publication at: <https://www.researchgate.net/publication/310111178>

Dynamics of a seafloor-spreading episode at the East Pacific Rise

Article in *Nature* · November 2016

DOI: 10.1038/nature20116

CITATIONS

3

READS

42

4 authors, including:



Yen Joe Tan

Columbia University

2 PUBLICATIONS 7 CITATIONS

[SEE PROFILE](#)



William Wilcock

University of Washington Seattle

134 PUBLICATIONS 2,620 CITATIONS

[SEE PROFILE](#)

Dynamics of a seafloor–spreading episode at the East Pacific Rise

Yen Joe Tan¹, Maya Tolstoy¹, Felix Waldhauser¹ & William S. D. Wilcock²

Seafloor spreading is largely unobserved because 98 per cent of the global mid-ocean-ridge system is below the ocean surface. Our understanding of the dynamic processes that control seafloor spreading is thus inferred largely from geophysical observations of spreading events on land at Afar in East Africa and Iceland¹. However, these are slow-spreading centres¹ influenced by mantle plumes^{2,3}. The roles of magma pressure and tectonic stress in the development of seafloor spreading are still unclear. Here we use seismic observations to show that the most recent eruption at the fast-spreading East Pacific Rise just North of the Equator initiated at a melt-rich segment about 5 kilometres long⁴. The change in static stress then promoted almost-concurrent rupturing along at least 35 kilometres of the ridge axis, where tectonic stress had built up to a critical level, triggering magma movement. The location of impulsive seismic events indicative of lava reaching the seafloor⁵ suggests that lava subsequently erupted from multiple isolated^{6,7} magma lenses (reservoir chambers) with variable magma ascent rates, mostly within 48 hours. Therefore, even at magmatically robust fast-spreading ridges, a substantial portion of the spreading may be due to tectonic stress building up to a critical level rather than magma overpressure in the underlying magma lenses.

The global mid-ocean ridge (MOR) system is located mostly in the deep ocean. Therefore, remote detections of seismic signals at submarine ridges are interpreted by analogy to observations at subaerial ridges to infer dynamic spreading processes. Only ten seafloor spreading events have been seismically characterized to date^{5,8}, with hydroacoustic detections of migrating earthquake swarms at intermediate-spreading ridges (about 4–9 cm yr⁻¹ at the full spreading rate) interpreted as lateral dike propagations⁹, similar to observations at slow-spreading centres (<4 cm yr⁻¹) in Afar and Iceland^{10–13}. However, less is known about fast-spreading ridges (>9 cm yr⁻¹), where the relatively thin lithosphere produces earthquakes that are extremely difficult to locate with existing hydroacoustic monitoring networks¹⁴.

The most recent eruption occurring near 9° 50' N at the fast-spreading East Pacific Rise is the first observed repeat eruption at a mid-ocean ridge^{15,16}. The event was recorded by ocean-bottom seismometers (OBSs) deployed between 9° 49' N and 9° 51' N from May 2005 to April 2006, although only three seismometers survived the lava flow and unrelated instrument failure. A dike event on 22 January 2006 was inferred from an hour-long peak in seismic amplitude¹⁶ and hydroacoustically detected (T-wave) earthquakes¹⁴. However, the eruption is widely referred to as the 2005–2006 eruption and cited as having happened in multiple pulses over a period of 7–10 months^{6,7,17,18} on the basis of radiometric dating results¹⁹, similar to the previous eruption at 9° 50' N in 1991–1992 (refs 15, 20). This implies that the eruptions were modulated by pulses of magma injection into the underlying axial magma lenses (AMLs).

We analysed the OBS data collected from May 2005 to April 2006 and detected three types of seismic events—impulsive lava events, local earthquakes, and long-period events (Figs 1 and 2). The lava events have impulsive waveforms with a dominant frequency around

22 Hz (Extended Data Fig. 1), similar to those previously suggested²¹ and recently confirmed to be associated with fresh lava reaching the seafloor⁵. This association is further supported by their locations (see Methods) which coincide extremely well with the fresh lava flow boundaries (Fig. 1b) mapped using digital seafloor imagery collected in 2006–2007 (ref. 17). Their spatiotemporal evolution, where events at individual flow lobes show initial migration away from the ridge axis before concentrating at the toe of the flows (Fig. 3, Extended Data Fig. 2a), is also consistent with lava freezing over as it reaches the seafloor and forming subsurface lava channels that allow subsequent flows to propagate off-axis¹⁵. These events could be generated by explosions from magma degassing²² or the interaction of lava with seawater²³ as lava reaches the seafloor, and are consistent with evidence for explosive activity at 9° 50' N during the 1991–1992 eruption¹⁵.

These lava events were detected starting 22 January 2006 and lasted for about a week, with about 85% of the located events occurring during the first two days (Extended Data Fig. 2b). This suggests that most of the lava erupted rapidly in the first 48 h and unequivocally dates the eruption to January 2006 rather than 2005–2006. With an estimated $22 \times 10^6 \text{ m}^3$ of lava erupted¹⁷, this gives an average eruption rate of around $100 \text{ m}^3 \text{ s}^{-1}$. This is much lower than the eruption rate of $10^3 \text{ m}^3 \text{ s}^{-1}$ to $10^6 \text{ m}^3 \text{ s}^{-1}$ derived from numerical modelling²⁴ for the less voluminous 1991–1992 eruption¹⁷, despite the melt from both eruptions being derived from the same mantle source⁷. Assuming that the lower eruption rate corresponds to a lower magma driving pressure, this suggests that tectonic stress may be important in initiating the 2006 eruption.

In the two years leading up to the eruption, earthquake activity rate gradually ramped up¹⁶. The limitations of the small surviving OBS array mean that our earthquake locations are largely restricted to within a small area between 9° 49.8' N and 9° 51.1' N and from the axial summit trough (AST) to approximately 2 km west of the axis (Fig. 1c). In the hours preceding the eruption, earthquakes in this area ruptured an eastward-dipping structure that goes down to approximately the depth of the AML near 9° 50.5' N (Extended Data Fig. 3). The structure might represent a zone of developing normal faults that were activated by the build-up of magma pressure⁷ or tectonic stress²⁵ since the last eruption. The build-up of stress is also indicated by the increasing magnitude of these local earthquakes in the hour preceding the volcanic crisis (Extended Data Fig. 4), which culminated in a cluster of T-wave earthquakes of body-wave magnitudes $M_b \approx 2\text{--}3.5$ near 9° 50.5' N (Fig. 1a) that was detected by a regional hydrophone array¹⁴.

Fifteen minutes after the first T-wave earthquakes near 9° 50.5' N, a series of long-period events were detected around the same region (Fig. 2). These signals have a dominant frequency around 1.6 Hz. Long-period events are regularly observed preceding volcanic eruptions and have been suggested to originate from a resonating source in a fluid-filled conduit or crack²⁶. These events are located (see Methods) west of the ridge axis within our seismic array (Fig. 1c). We did not find any long-period events that are not detected by all stations. This suggests that similar signals are unlikely to occur just outside the array.

¹Lamont-Doherty Earth Observatory of Columbia University, Palisades, New York 10964, USA. ²School of Oceanography, University of Washington, Seattle, Washington 98195, USA.

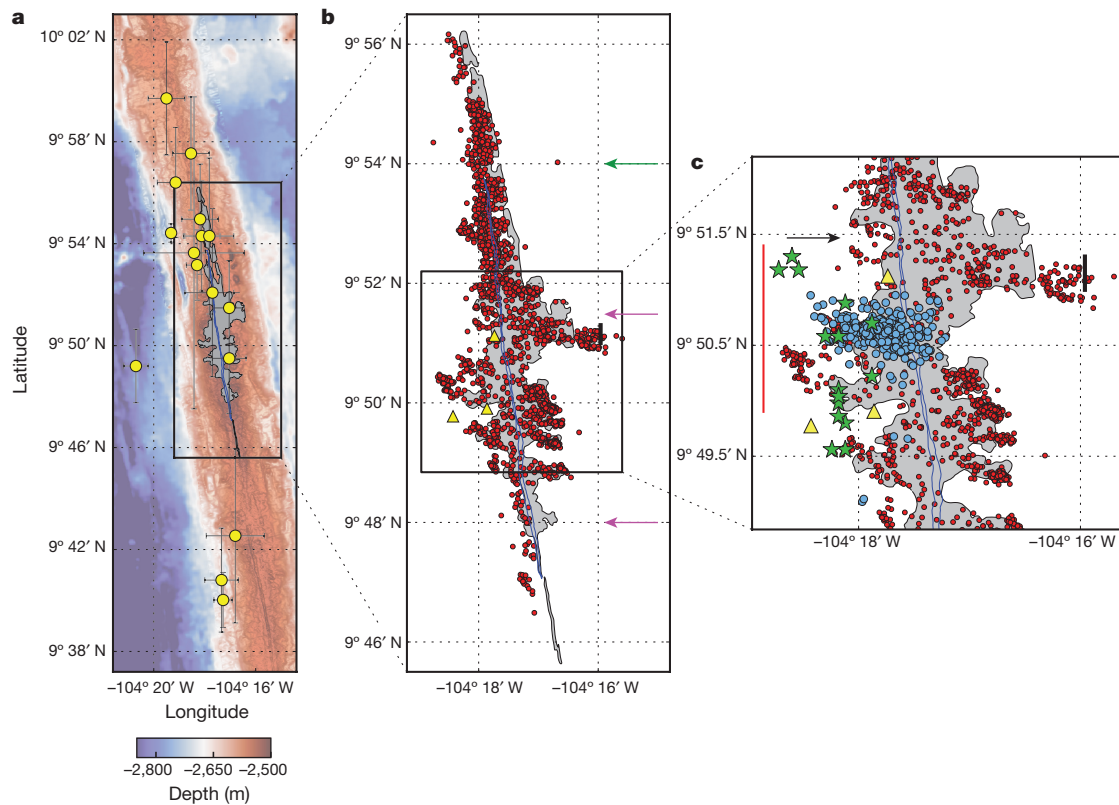


Figure 1 | Location of various seismic events. **a**, Location of T-wave earthquakes¹⁴ (yellow dots) and lava flow map¹⁷ (shaded region). Error bars represent 68% confidence interval¹⁴. **b**, Location of seismometers (yellow triangles) and impulsive lava events (red dots), showing close spatial correlation with the lava flow map¹⁷. The AST¹⁷ is shown as a thin blue line with green arrow marking its end. The bold black line marks the revised extent of the 2006 lava flow farther off-axis than originally

identified¹⁸. AML disruptions (purple arrows) were inferred from seismic reflection studies post-eruption⁶. **c**, Location of impulsive lava events (red dots), local earthquakes (blue dots), and long-period events (green stars). The black arrow marks the break in AST and the northern extent of melt-depleted sub-AML³⁰ (red line) associated with the end of the northward migration of long-period events. The bold black line marks the revised extent of the 2006 lava flow farther off-axis than originally identified¹⁸.

These long-period events are the largest-amplitude signals detected by the OBSs throughout their deployment. Seismic reflection studies after the eruption have shown melt bodies up to a kilometre off-axis in the region²⁷. Therefore, these long-period events might reflect dike initiation from the western edge of the AML, consistent with models that suggest that diking might initiate at the edge of a magma lens²⁸. The first T-wave earthquakes occurred before the long-period events, which suggests that the faults could have breached through to the AML and initiated magma movement²⁵.

The long-period events started near 9° 49.5' N and migrated about 4 km northward over the next 30 min, terminating at 9° 51.3' N near a break in the AST¹⁷ and the AML⁶ (Figs 1c and 2). These events may reflect flow instabilities as magma rises vertically from the magma lens while the AML ruptures northward (Fig. 4), or lateral dike propagation along the segment that terminated at a stress barrier²⁹. The along-axis extent of long-period events matches that of the melt-depleted section of a deeper magma lens (sub-AML) underlying the top AML (Figs 1c and 2) imaged post-eruption³⁰. This suggests that the rapid draining of this segment of the AML might have induced recharge from the underlying sub-AML³⁰ (Fig. 4). Lava first reached the seafloor in this region around 2 h after the first T-wave earthquakes (Fig. 2). This implies that magma rose from the AML starting at a depth of around 1.5 km (ref. 6) at a rate of about 0.21 m s⁻¹ (see Methods). The seismicity in this central segment peaked and stopped before the start of the long-period events swarm (Fig. 2). This suggests that the spreading episode started with faulting that triggered magma movement, and not the reverse. This is different from the 1978 Krafla event, where the main earthquake swarm started after a peak in continuous tremor¹¹, and from the 2005 Afar event, where earthquake swarms continued after a peak in sporadic tremors and ultralong-period events¹².

The T-wave earthquakes subsequently clustered to the south and north of 9° 50.5' N (Fig. 2), encompassing the entire eruption area and beyond¹⁴. This is unlikely to represent lateral dike propagation because that would require an unrealistic propagation rate of approximately 14–32 m s⁻¹ (ref. 14). Therefore, we infer that the earthquake clustering reflects almost-concurrent faulting that was probably promoted by the static stress change from the diking event near 9° 50.5' N. This suggests that the plate boundary was close to failure owing to the build-up of tectonic stress over the 14 years or so since its last spreading episode²⁵. Our observation differs from those at spreading episodes at Afar and Iceland, where dikes propagated laterally for tens of kilometres over multiple weeks^{10–13}. Although these T-wave earthquakes were the largest earthquakes in the region during this period, we were not able to identify them on the OBSs, probably owing to the high seismic noise amplitude during this period and their locations farther away and outside our OBS array (Fig. 2).

The rupturing of the ridge axis then triggered vertical magma movement from the underlying, segmented AMLs^{6,7} (Fig. 4). Immediately after lava first reached the seafloor at the central segment between 9° 49' N and 9° 51' N, impulsive lava events at the adjacent segment to the north show a northward migration of about 5 km at a rate of 1.07 m s⁻¹, terminating at the end of the AST¹⁷ (Fig. 2). This reflects either dike propagation triggered by rupturing of the ridge axis or lava flowing northward within the AST. About 45 min later, lava started erupting in the northernmost region (Fig. 2) from off-axis fissures approximately 600 m east of the AST¹⁷, fed by a different AML⁷. The northernmost region has a slower inferred magma ascent rate of about 0.14 m s⁻¹ (see Methods).

The location of the first T-wave earthquakes and long-period events suggests that the eruption initiated near 9° 50.5' N. This region has the

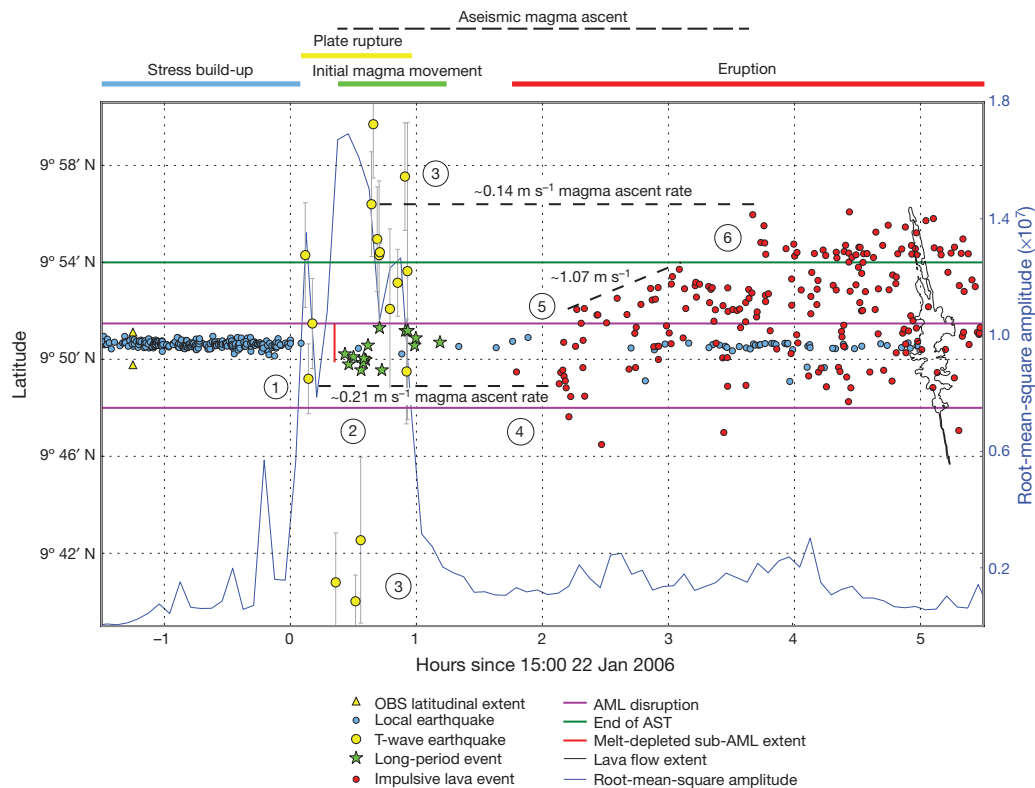


Figure 2 | Temporal and along-axis progression of various seismic events. (1) Build-up of stress culminating in plate rupture. (2) This triggered magma movement from the underlying melt-rich AML. (3) The static stress change then promoted rupturing beyond the initiation region. (4) Lava first erupted in the central segment. (5) Lava then erupted from a different AML⁶ at the adjacent segment. (6) Finally, the rupturing triggered magma from another isolated⁷ AML to rise vertically at a slower speed and erupt with a smaller volume. T-wave earthquake error bars represent the 68% confidence interval¹⁴. Magma ascent rates were calculated assuming an AML depth of 1.5 km (see Methods). AML disruptions (purple horizontal lines) and extent of melt-depleted

sub-AML (red vertical line) were inferred from seismic reflection studies post-eruption^{6,30}. New lava flow extent (solid black line), shown in map view for reference, was mapped post-eruption¹⁷. The root-mean-square amplitude of the seismic vertical channel was calculated in the 3–45-Hz band in 5-min windows (blue line). Note that flows from ~9° 48' N to ~9° 46' N did not overflow the AST and are associated with very few impulsive lava events. The southernmost T-wave earthquakes are consistent with the possible disruption of vent fluid temperatures at 9° 42' N (ref. 17). This suggests that spreading occurred along about 35 km of the ridge axis. However, spreading could have extended beyond the distal ends of the observed T-wave earthquakes.

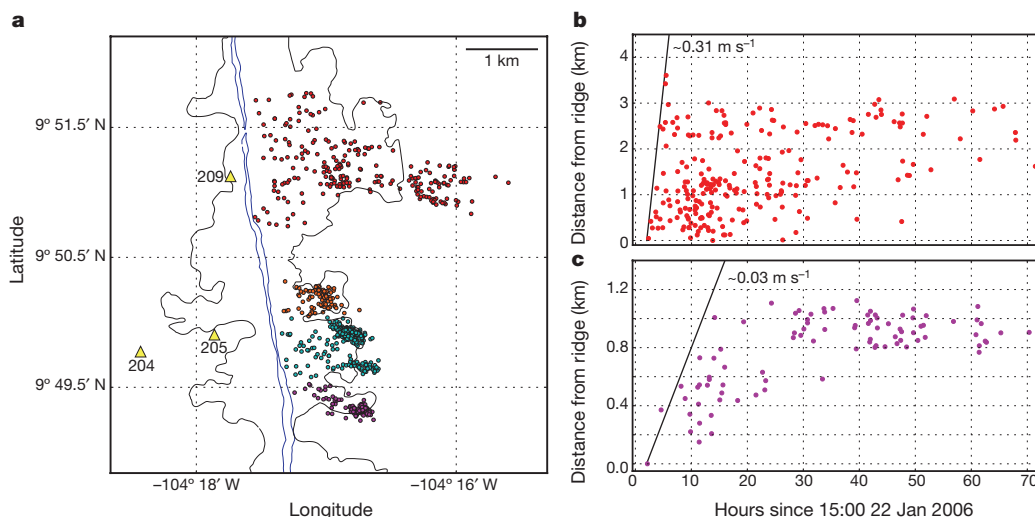


Figure 3 | Lava flow velocities. **a**, Location of seismometers (yellow triangles labelled with station numbers) and impulsive lava events (coloured dots) in the four flow lobes¹⁷ (thin black outline enclosing the lava flow). The AST¹⁷ is shown as a thin blue line. **b**, **c**, Impulsive lava events in the northernmost flow lobe propagated farther off-axis at a faster rate than events in the southernmost flow lobe. At later times, events were

concentrated at the toe (on the right) of the flows. Migration of other flow lobe events is shown in Extended Data Fig. 5. No spatiotemporal trend was observed for the flow to the west of the ridge axis, possibly because we missed many events in the first hour of the eruption (see Methods). The first events we located in the western flow lobe are already more than a kilometre off-axis (Extended Data Fig. 2a).

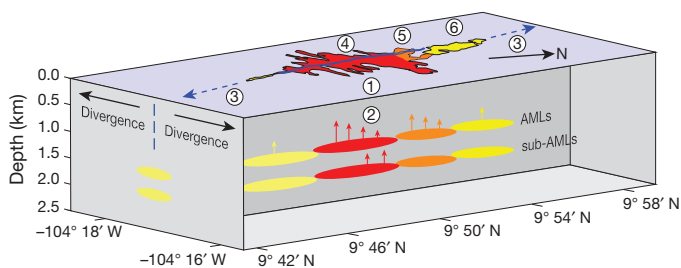


Figure 4 | Schematic representation of the dynamics of seafloor spreading at the East Pacific Rise. Numbers 1–6 mark the inferred processes represented in Fig. 2. (1) Build-up of stress culminated in plate rupture (T-wave earthquakes). (2) This triggered magma movement (long-period events) from the underlying melt-rich AML (red ellipse) which then induced recharge from a deeper sub-AML³⁰. (3) The static stress change then promoted rupturing (clustering of T-wave earthquakes) beyond the initiation region (blue dashed arrows) owing to the build-up of tectonic stress to a critical level at the plate boundary. (4) Lava first erupted (impulsive lava events) in the central segment. (5) Lava then erupted from a different AML⁶ (orange ellipse) at the adjacent segment. (6) Finally, the rupturing triggered magma from another isolated⁷ AML (yellow ellipse) to rise vertically at a slower speed and erupt with a smaller volume.

highest density of active high-temperature hydrothermal venting³¹, is near the location of the largest flow lobe from this eruption¹⁷, overlies a drained sub-AML imaged post-eruption³⁰, and has generally been considered the focus of magmatic activity and upwelling. The lavas from this region also have the highest MgO lava compositions of this eruption, suggesting relatively hot melt in the underlying AML⁷. The impulsive lava events from the flow lobe near this region propagated farthest off-axis at the fastest speed of about 0.31 m s^{-1} (Fig. 3b) compared to the events in the smaller lobes to the south that propagated at about 0.03 m s^{-1} (Fig. 3c, Extended Data Fig. 5b and c). This shows that this region had the highest lava effusion rate during the eruption, consistent with the presence of high-flow-rate morphologies¹⁸. Post-eruption seismic imaging showed that the AML underneath this 5-km-long segment is the most melt-depleted⁴, indicating that this is where most of the erupted lava was sourced from. Geochemical modelling suggests that the spreading episode was not triggered by renewed injection of magma into the underlying AML⁷, unlike at Krafla in 1978 and at Dabbahu in 2005 (ref. 1). However, the initiation at this segment may be due to long-term build-up of magma pressure⁷ or tectonic stress²⁵ since the last eruption.

Static stress change associated with the diking then promoted almost-concurrent rupturing along at least 35 km of ridge axis, triggering eruption of melt sourced from multiple AMLs^{6,7}. The less voluminous flows north of $9^{\circ} 54' \text{ N}$ and south of $9^{\circ} 48' \text{ N}$ (Fig. 1b), where lava did not even flow over the AST¹⁷, might reflect a relatively lower magma driving pressure from the underlying, isolated AMLs. Disruption in vent temperatures as far south as $9^{\circ} 42' \text{ N}$ (ref. 17) suggests that faulting may have happened even farther south without lava reaching the surface, consistent with the southernmost T-wave earthquakes on 22 January 2006.

The variable along-axis magma ascent rates and erupted lava volumes support that the multiple underlying AMLs are segmented⁶ and thus unlikely to be concurrently critically stressed from build-up of magma pressure. Instead, the build-up of tectonic stress to a critical level probably allowed almost-concurrent faulting along at least 35 km of the ridge segment, which then triggered magma movement. This is consistent with a model in which the AMLs are surrounded by hot asthenosphere and hence too weak to maintain large magma overpressure or support large elastic stress differences from the low strain rate of plate pull. The high strain rate of faulting is thus needed to breach through to the AMLs to trigger magma movement²⁵. Therefore, we can conclude that spreading along at least 30 km of the 35-km-long ridge segment (>85%) happened owing to build-up of tectonic stress.

If plate pull dominates at this magmatically robust fast-spreading ridge, it could also dominate at intermediate- and slow-spreading ridges, which generally have relatively lower magma supplies. Therefore, while MORs are often described as volcanoes that erupt owing to build-up of magma pressure^{7,19}, our study demonstrates that eruptions at MORs are a fundamentally different process largely controlled by tectonic stress due to plate pull. MORs could be viewed less as volcanoes and more as tears in the crust where magma reaches the surface when plates are pulled apart.

Online Content Methods, along with any additional Extended Data display items and Source Data, are available in the online version of the paper; references unique to these sections appear only in the online paper.

Received 23 March; accepted 26 September 2016.

Published online 14 November 2016.

- Wright, T. J. *et al.* Geophysical constraints on the dynamics of spreading centres from rifting episodes on land. *Nat. Geosci.* **5**, 242–250 (2012).
- Ebinger, C. J. & Sleep, N. H. Cenozoic magmatism throughout east Africa resulting from impact of a single plume. *Nature* **395**, 788–791 (1998).
- Wolfe, C. J., Bjarnason, I. T. H., Vandecar, J. C. & Solomon, S. C. Seismic structure of the Iceland mantle plume. *Nature* **385**, 245–247 (1997).
- Xu, M. *et al.* Variations in axial magma lens properties along the East Pacific Rise ($9^{\circ} 30' \text{ N}$ – $10^{\circ} 00' \text{ N}$) from swath 3-D seismic imaging and 1-D waveform inversion. *J. Geophys. Res.* **119**, 2721–2744 (2014).
- Wilcock, W. S. D., Tolstoy, M., Garcia, C., Tan, Y. J. & Waldhauser, F. Live from the seafloor: seismic signals associated with the 2015 eruption of Axial Seamount. *Eos* **OS41B–07** (2015).
- Carbotte, S. M. *et al.* Fine-scale segmentation of the crustal magma reservoir beneath the East Pacific Rise. *Nat. Geosci.* **6**, 866–870 (2013).
- Goss, A. R. *et al.* Geochemistry of lavas from the 2005–2006 eruption at the East Pacific Rise, $9^{\circ} 46' \text{ N}$ – $9^{\circ} 56' \text{ N}$: implications for ridge crest plumbing and decadal changes in magma chamber compositions. *Geochem. Geophys. Geosyst.* **11**, Q05T09 (2010).
- Tolstoy, M. Mid-ocean ridge eruptions as a climate valve. *Geophys. Res. Lett.* **42**, 1346–1351 (2015).
- Dziak, R. P. *et al.* Rapid dike emplacement leads to eruptions and hydrothermal plume release during seafloor spreading events. *Geology* **35**, 579–582 (2007).
- Abdallah, A. *et al.* Relevance of Afar seismicity and volcanism to the mechanics of accreting plate boundaries. *Nature* **282**, 17–23 (1979).
- Einarsson, P. & Brandsdóttir, B. Seismological evidence for lateral magma intrusion during the July 1978 deflation of the Krafla volcano in NE Iceland. *J. Geophys.* **47**, 160–165 (1980).
- Ayele, A. *et al.* September 2005 mega-dike emplacement in the Manda-Harrano nascent oceanic rift (Afar depression). *Geophys. Res. Lett.* **36**, L20306 (2009).
- Sigmundsson, F. *et al.* Segmented lateral dyke growth in a rifting event at Bárðarbunga volcanic system, Iceland. *Nature* **517**, 191–195 (2014).
- Dziak, R. P. *et al.* January 2006 seafloor-spreading event at $9^{\circ} 50' \text{ N}$, East Pacific Rise: ridge dike intrusion and transform fault interactions from regional hydroacoustic data. *Geochem. Geophys. Geosyst.* **10**, Q06T06 (2009).
- Haymon, R. M. *et al.* Volcanic eruption of the mid-ocean ridge along the East Pacific Rise crest at $9^{\circ} 45' \text{ N}$ – $52' \text{ N}$: direct submersible observations of seafloor phenomena associated with an eruption event in April, 1991. *Earth Planet. Sci. Lett.* **119**, 85–101 (1993).
- Tolstoy, M. *et al.* A sea-floor spreading event captured by seismometers. *Science* **314**, 1920–1922 (2006).
- Soule, S. A., Fornari, D. J., Perfit, M. R. & Rubin, K. H. New insights into mid-ocean ridge volcanic processes from the 2005–2006 eruption of the East Pacific Rise, $9^{\circ} 46' \text{ N}$ – $9^{\circ} 56' \text{ N}$. *Geology* **35**, 1079–1082 (2007).
- Fundis, A. T., Soule, S. A., Fornari, D. J. & Perfit, M. R. Paving the seafloor: Volcanic emplacement processes during the 2005–2006 eruptions at the fast spreading East Pacific Rise, $9^{\circ} 50' \text{ N}$. *Geochem. Geophys. Geosyst.* **11**, Q08O24 (2010).
- Rubin, K. H. *et al.* Volcanic eruptions in the deep sea. *Oceanography (Wash. D.C.)* **25**, 142–157 (2012).
- Rubin, K. H., Macdougall, J. D. & Perfit, M. R. ^{210}Po – ^{210}Pb dating of recent volcanic eruptions on the sea floor. *Nature* **368**, 841–844 (1994).
- Schlindwein, V., Muller, C. & Jokat, W. Seismoacoustic evidence for volcanic activity on the ultraslow spreading Gakkel Ridge, Arctic Ocean. *Geophys. Res. Lett.* **32**, L18306 (2005).
- Vergnolle, S., Brandeis, G. & Mareschal, J. C. Strombolian explosions. 2. Eruption dynamics determined from acoustic measurements. *J. Geophys. Res.* **101**, 20449–20466 (1996).
- Perfit, M. R. *et al.* Interaction of sea water and lava during submarine eruptions at mid-ocean ridges. *Nature* **426**, 62–65 (2003).
- Gregg, T. K. P., Fornari, D. J., Perfit, M. R., Haymon, R. M. & Fink, J. H. Rapid emplacement of a mid-ocean ridge lava flow on the East Pacific Rise at $9^{\circ} 46' \text{ N}$ – $51' \text{ N}$. *Earth Planet. Sci. Lett.* **144**, E1–E7 (1996).
- Buck, W. R. On the frequency of dike intrusion episodes at spreading centers. *Eos* **T41B–1566** (2006).
- Chouet, B. A. Long-period volcano seismicity: its source and use in eruption forecasting. *Nature* **380**, 309–316 (1996).

27. Canales, J. P. *et al.* Network of off-axis melt bodies at the East Pacific Rise. *Nat. Geosci.* **5**, 279–283 (2012).
28. Bohnenstiehl, D. R. & Carbotte, S. M. Faulting patterns near 19°30'S on the East Pacific Rise: fault formation and growth at a superfast spreading center. *Geochem. Geophys. Geosyst.* **2**, 1056 (2001).
29. Buck, W. R., Einarsson, P. & Brandsdottir, B. Tectonic stress and magma chamber size as controls on dike propagation: constraints from the 1975–1984 Krafla rifting episode. *J. Geophys. Res.* **111**, B12404 (2006).
30. Marjanović, M. *et al.* A multi-sill magma plumbing system beneath the axis of the East Pacific Rise. *Nat. Geosci.* **7**, 825–829 (2014).
31. Fornari, D. *et al.* in *The Thermal Structure of the Ocean Crust and the Dynamics of Hydrothermal Circulation* Vol. 148, 187–218 (AGU Geophys. Monogr., American Geophysical Union, 2004).

Acknowledgements Y.J.T. thanks W. R. Buck for discussions and reading of the manuscript. Y.J.T. thanks A. H. Barclay and R. S. Matoza for discussions.

We thank R. P. Dziak and D. R. Bohnenstiehl for providing the T-wave earthquake catalogue. We thank the captains, crews and science parties of the RV *Knorr* and RV *Atlantis*. This work was supported by NSF grant OCE-0961594.

Author Contributions Y.J.T., advised by M.T. and F.W., analysed the seismic data and wrote the manuscript. M.T. and F.W. conceived and ran the experiment. W.S.D.W.'s identification of impulsive lava signals at Axial inspired this study. All authors discussed the results and commented on the manuscript.

Author Information Reprints and permissions information is available at www.nature.com/reprints. The authors declare no competing financial interests. Readers are welcome to comment on the online version of the paper. Correspondence and requests for materials should be addressed to Y.J.T. (yjt@ldeo.columbia.edu).

Reviewer Information *Nature* thanks J. Karson and V. Schlindwein for their contribution to the peer review of this work.

METHODS

Impulsive lava event detection and location. We used a standard detection algorithm based on short-term average to long-term average of the seismic energy recorded by the seismometer, covering May 2005 to April 2006. We then manually went through the entire period to identify missed events and to pick the arrivals. No events were identified before 22 January 2006. During the first hour of the eruption, we could not locate all the events because many of them were occurring simultaneously at short distances from the stations, thus observed phases could not be uniquely assigned to individual events.

Events were located by assuming the signals were generated on the seafloor and had bounced off the sea surface once before reaching the seismometers (Extended Data Fig. 2b inset). We used an iterative least-squares method assuming a constant sound velocity of 1.5 km s^{-1} with water depth from a high-resolution bathymetry map acquired in November 2005 (ref. 32). The sound velocity profile with depth in this region varies from 1.48 km s^{-1} to 1.52 km s^{-1} (ref. 33). We quantify our location uncertainties due to a simplified sound velocity model by locating the events with a sound velocity of 1.48 km s^{-1} and 1.52 km s^{-1} . This shifts our original catalogue locations by an average of 107 m. We quantify our location uncertainties due to pick error by adding normally distributed noise of standard deviation 0.1 s to the arrival times before locating the events. This is performed on the whole catalogue 100 times. On average, the event locations are shifted by $<1 \text{ m}$. This small uncertainty may be explained by the slow sound velocity, as the locations are well constrained by the station relative arrival times (on the order of seconds, which is much larger than the estimated pick error of 0.1 s). Event magnitudes were calculated as the logarithm of the displacement (in micrometres) multiplied by the signal travel distance (in kilometres). This assumes no attenuation other than from geometric spreading.

Earthquake detection and location. We manually went through a 6.5-h period starting from approximately 3 h before the first impulsive lava event was identified and handpicked the P- and S-wave arrivals. This was the period of highest seismic root-mean-square amplitude during the deployment¹⁶. These events were then used as templates for an array-based waveform correlation detection algorithm³⁴. We then manually reviewed the detected events. Events with both P- and S-wave arrivals at all three stations were located using the NonLinLoc grid-search program³⁵. A window of 0.5 s around each arrival was extracted for cross-correlation to get differential arrival times. Only differential arrival times with cross-correlation coefficient above 0.7 were used in the relocation using the hypoDD program³⁶. Depth-dependent P- and S-wave one-dimensional velocity models were used³⁷. Local magnitudes (M_L) were derived using the formulation described in ref. 38. Synthetic test suggests that the eastward dipping structure we observed is resolvable (Extended Data Fig. 6). Least-squares errors for the relative locations were computed³⁶ using a subset of better-constrained events (template events and events located within the OBS array). The mean relative location errors are 120 m for longitude, 40 m for latitude, and 220 m for depth (Extended Data Fig. 7).

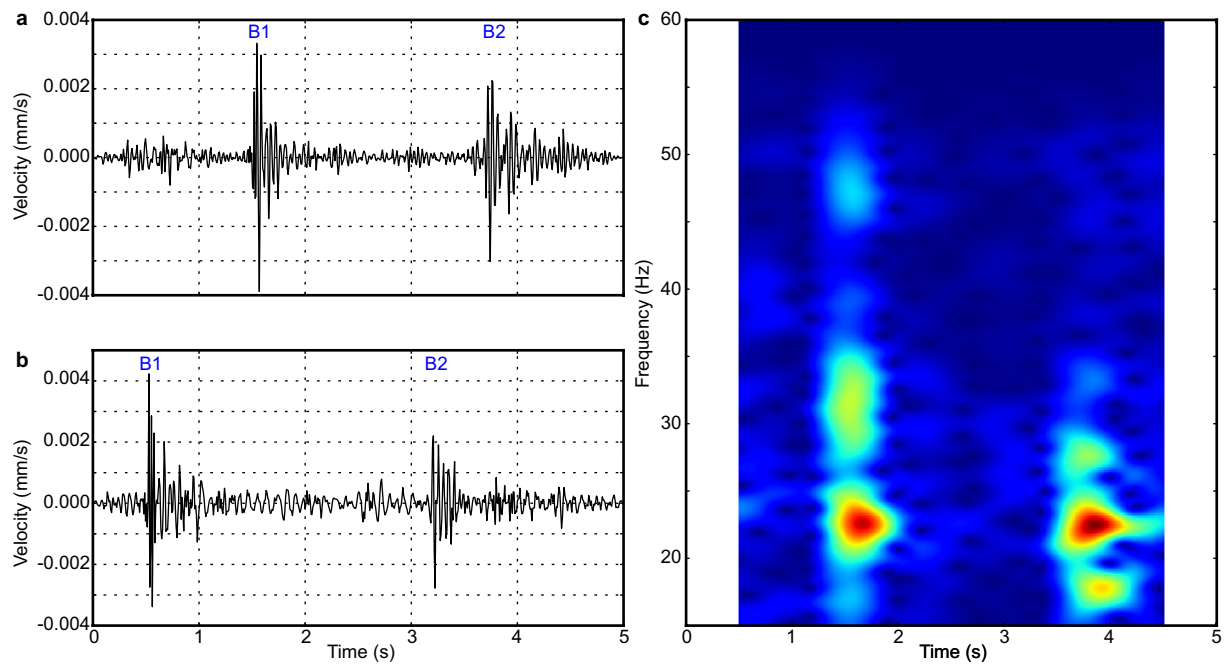
Long-period event detection and location. We manually picked the first arrivals and located the events using a grid search method that minimizes the standard deviation of predicted source origin times based on arrival times at each station³⁹, assuming a fixed source depth and constant velocity of 2.5 km s^{-1} . A 100-m grid spacing was used. The epicentres of the events do not change very much between the assumed depths of 0 km to 1.5 km (Extended Data Fig. 8a), which is the approximate depth of the AML⁶. Velocities between 0.5 km s^{-1} and 6.5 km s^{-1} were tested, with the velocity of 2.5 km s^{-1} giving the overall minimum standard deviation

(Extended Data Fig. 9). This velocity is consistent with a mean crustal S-wave velocity above 1.5 km depth³⁷. However, the epicentres of the events do not change very much with change in velocity assumption (Extended Data Fig. 8b), because the northward migration of the event locations is constrained by the station relative arrival time (Extended Data Fig. 10).

Magma ascent rates calculation. For the northernmost segment, the AML depth varies from 1.5 km to 1.65 km (ref. 6). The time gap between the first T-wave earthquake and the first lava event in this region is about 181 min. Therefore, the calculated magma ascent rate is between 0.14 m s^{-1} and 0.15 m s^{-1} . For the central segment, the AML depth varies from 1.45 km to 1.6 km (ref. 6). The time gap between the first T-wave earthquake and the first cluster of lava events in this region is about 117 min (Fig. 2). Therefore, the calculated magma ascent rate is between 0.21 m s^{-1} and 0.23 m s^{-1} . However, there is a single lava event that happened about 97 min after the first T-wave earthquake in this region (Fig. 2). If this event time is used instead, the calculated magma ascent rate for the central segment is between 0.25 m s^{-1} and 0.28 m s^{-1} . This event time represents a conservative estimate for the earliest lava event in the central segment because, at the start of the eruption, many events were occurring simultaneously at short distances from the stations, so that observed phases could not be uniquely assigned to individual events. The time gap between the last long-period event and the first lava event is around 36 min. If this aseismic period is the time of magma ascent instead, it would give the fastest rate of between 0.67 m s^{-1} and 0.74 m s^{-1} .

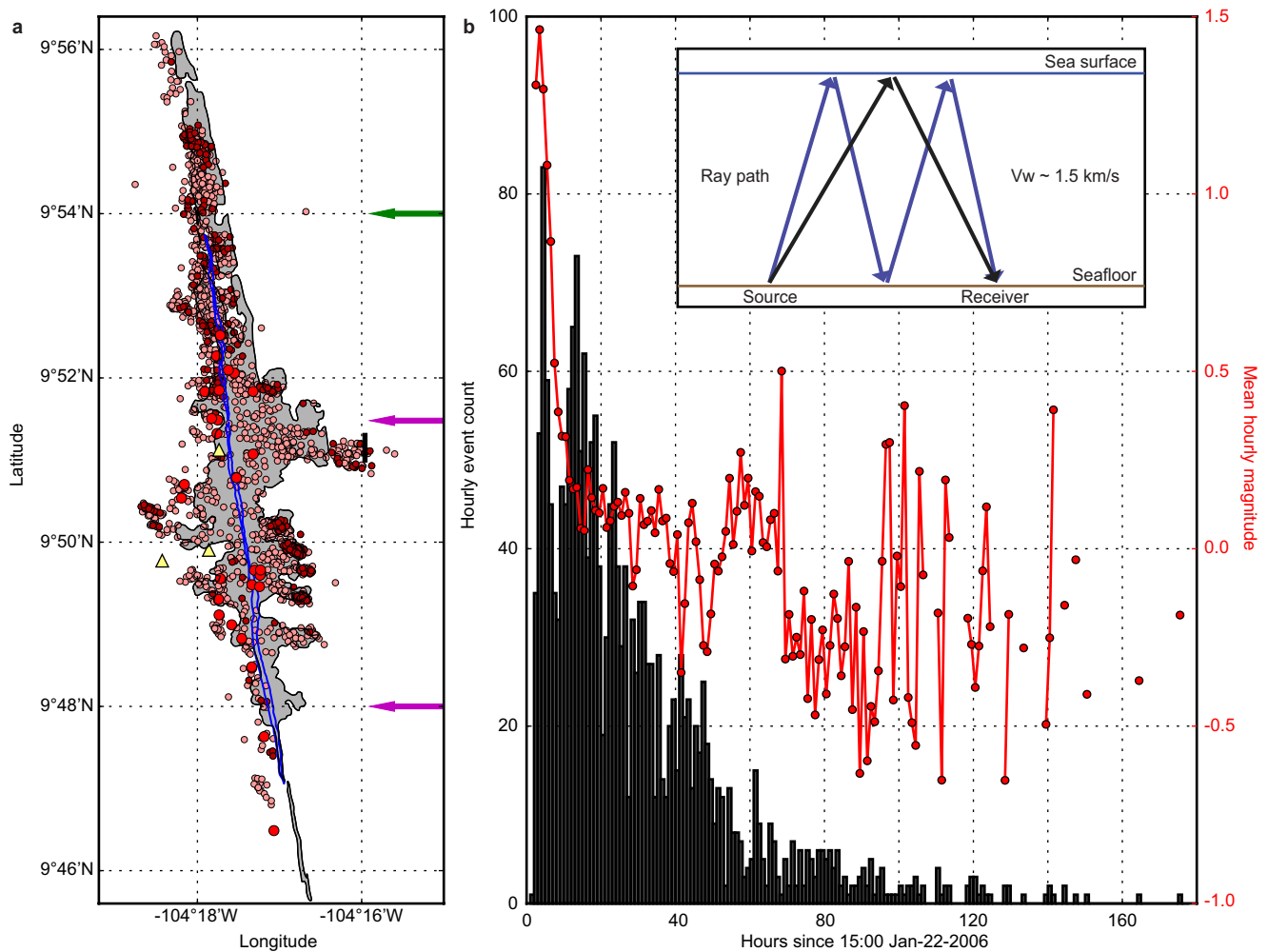
Data availability. Source data for Figs 1b and c, 2 and 3 and Extended Data Figs 2–5 are provided with the online version of the paper. All other data supporting the findings of this study are available from the corresponding author upon request.

32. White, S. M., Haymon, R. M. & Carbotte, S. A new view of ridge segmentation and near-axis volcanism at the East Pacific Rise, 8° – 12°N , from EM300 multibeam bathymetry. *Geochem. Geophys. Geosyst.* **7**, Q12005 (2006).
33. Munk, W. H., Worcester, P. & Wunsch, C. The forward problem: range-independent. *Ocean Acoust. Tomogr.* 30–114 (1995).
34. Gibbons, S. J. & Ringdal, F. The detection of low magnitude seismic events using array-based waveform correlation. *Geophys. J. Int.* **165**, 149–166 (2006).
35. Lomax, A., Michelini, A. & Curtis, A. Earthquake location, direct, global-search methods in *Encyclopedia of Complexity and System Science* Vol. 1, 2449–2473 (Springer, 2009).
36. Waldhauser, F. & Ellsworth, W. L. A double-difference earthquake location algorithm: Method and application to the Northern Hayward Fault, California. *Bull. Seismol. Soc. Am.* **90**, 1353–1368 (2000).
37. Waldhauser, F. & Tolstoy, M. Seismogenic structure and processes associated with magma inflation and hydrothermal circulation beneath the East Pacific Rise at $9^{\circ}50'\text{N}$. *Geochem. Geophys. Geosyst.* **12**, Q08T10 (2011).
38. Bohnenstiehl, D. R., Waldhauser, F. & Tolstoy, M. Frequency-magnitude distribution of microearthquakes beneath the $9^{\circ}50'\text{N}$ region of the East Pacific Rise, October 2003 through April 2004. *Geochem. Geophys. Geosyst.* **9**, Q10T03 (2008).
39. Gottschämer, E. & Surono, I. Locating tremor and shock sources recorded at Bromo Volcano. *J. Volcanol. Geotherm. Res.* **101**, 199–209 (2000).
40. Saal, A. E., Hauri, E. H., Langmuir, C. H. & Perfit, M. R. Vapour undersaturation in primitive mid-ocean-ridge basalt and the volatile content of Earth's upper mantle. *Nature* **419**, 451–455 (2002).
41. Shinohara, H. Excess degassing from volcanoes and its role on eruptive and intrusive activity. *Rev. Geophys.* **46**, RG4005 (2008).
42. Soule, S. A. *et al.* CO_2 variability in mid-ocean ridge basalts from syn-emplacement degassing: constraints on eruption dynamics. *Earth Planet. Sci. Lett.* **327–328**, 39–49 (2012).



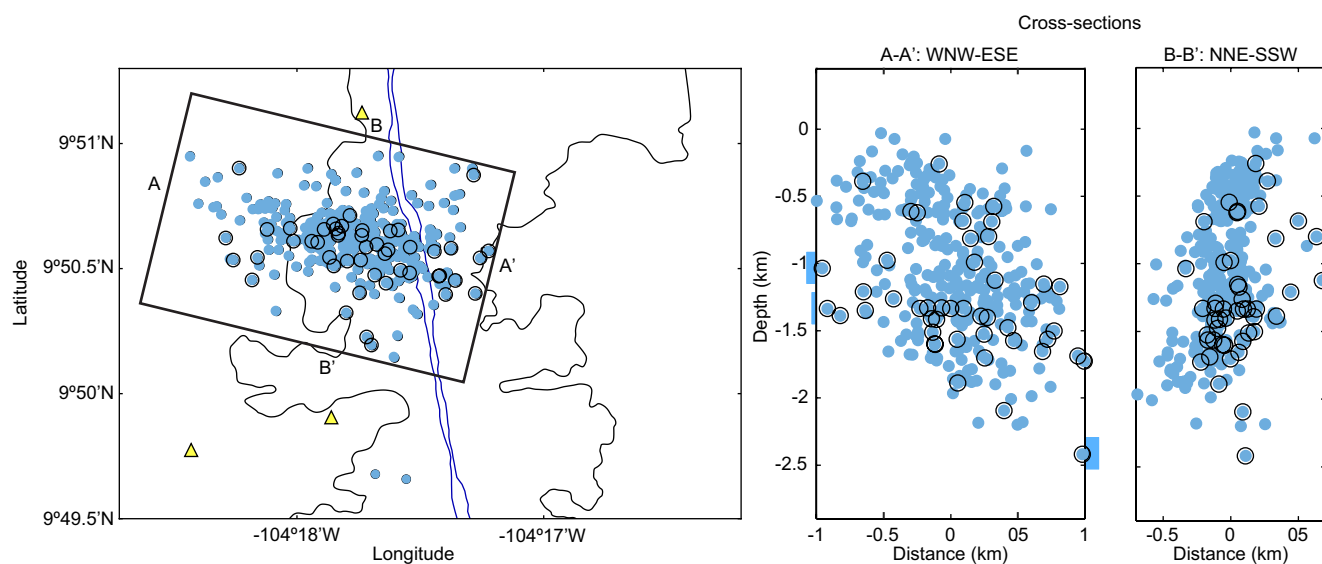
Extended Data Figure 1 | Impulsive lava event signals. **a, b,** Velocity seismograms of the same event recorded at two different stations. The difference in station relative arrival time of >1 s for the first arrival suggests a waterborne arrival (that is, the seismic wave travelled through the water column rather than through the crust), since these stations are around 2 km apart, with water velocity being 1.5 km s^{-1} and P-wave

crustal velocity being around $4\text{--}5 \text{ km s}^{-1}$ (ref. 37). The event also has multiple arrivals: the first arrival represents a signal that has bounced off the sea surface once (B1) and the second arrival represents a signal that has bounced off the sea surface twice (B2) (Extended Data Fig. 2b). **c,** The signal shows a dominant frequency of about 22 Hz.



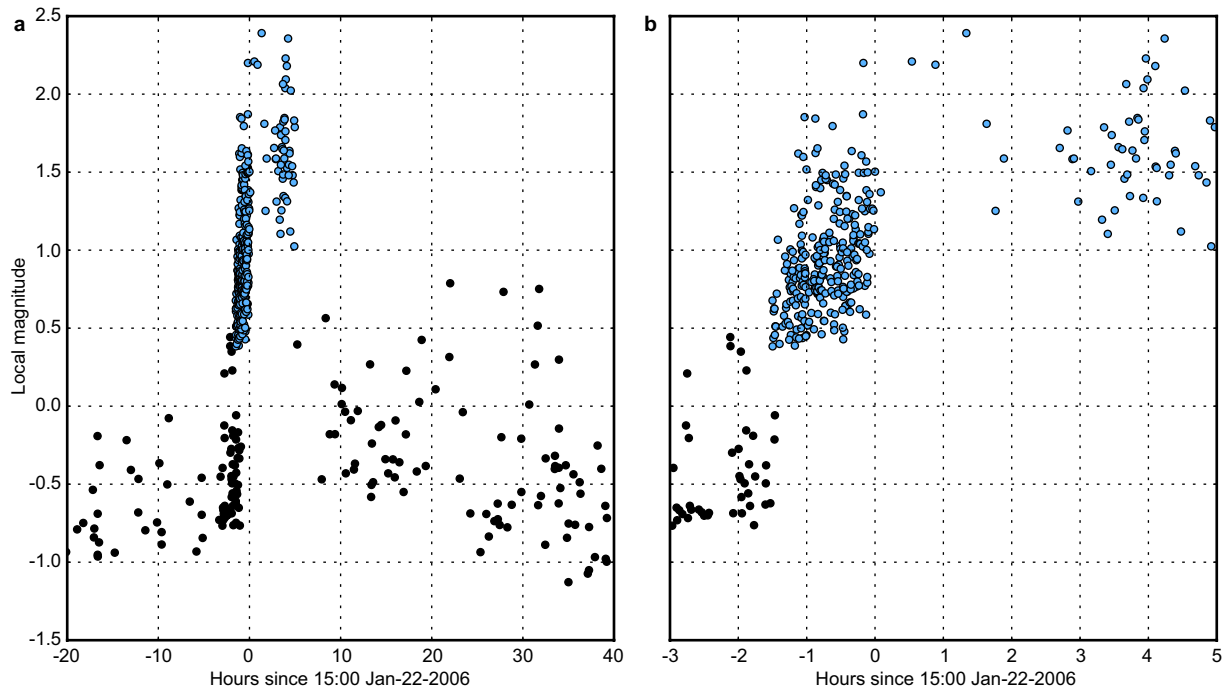
Extended Data Figure 2 | Impulsive lava events. **a**, Location of seismometers (yellow triangles) and impulsive lava events in the first hour (red), first two days (pale red), and last five days (dark red). The AST¹⁷ is shown as a thin blue line with green arrow marking its end. The bold black line marks revised 2006 lava flow farther off-axis than originally identified¹⁸. AML disruptions (purple arrows) were inferred from seismic reflection studies post-eruption⁶. **b**, Histogram of hourly impulsive lava event rate. The red line shows hourly average impulsive lava event magnitude. Mid-ocean-ridge basalt on the East Pacific Rise has been found to have low volatile content⁴⁰. Therefore, the larger-magnitude impulsive lava events during the first 5 h might be driven by excess degassing of volatiles from a larger reservoir of unerupted magma⁴¹, consistent with the estimate that <15% of the available magma in the AML was erupted¹⁷.

The lava has also been suggested to have degassed from supersaturated conditions owing to a rapid magma ascent rate from depth⁴². The breaks in the red line are due to hours when there are no events located, and hence no average magnitude data point. Event magnitudes were calculated as the logarithm of the displacement (in micrometres) multiplied by the signal travel distance (in kilometres), which is different from earthquake magnitude. The inset shows the model of the signal travel path used in locating the impulsive lava events (V_w is the velocity of the seismic wave travelling through the water column). A direct waterborne arrival is not recorded, probably because of the upward refraction of energy due to increasing velocity with water depth. The lack of crustal arrival indicates a small absolute magnitude.



Extended Data Figure 3 | Earthquake locations. The A–A' depth slice shows a 1-km-thick east-southeast (ESE)-dipping structure towards the ridge axis. The B–B' depth slice shows that the structure is subvertical in this direction (that is, north-northeast to south-southwest, NNE–SSW)

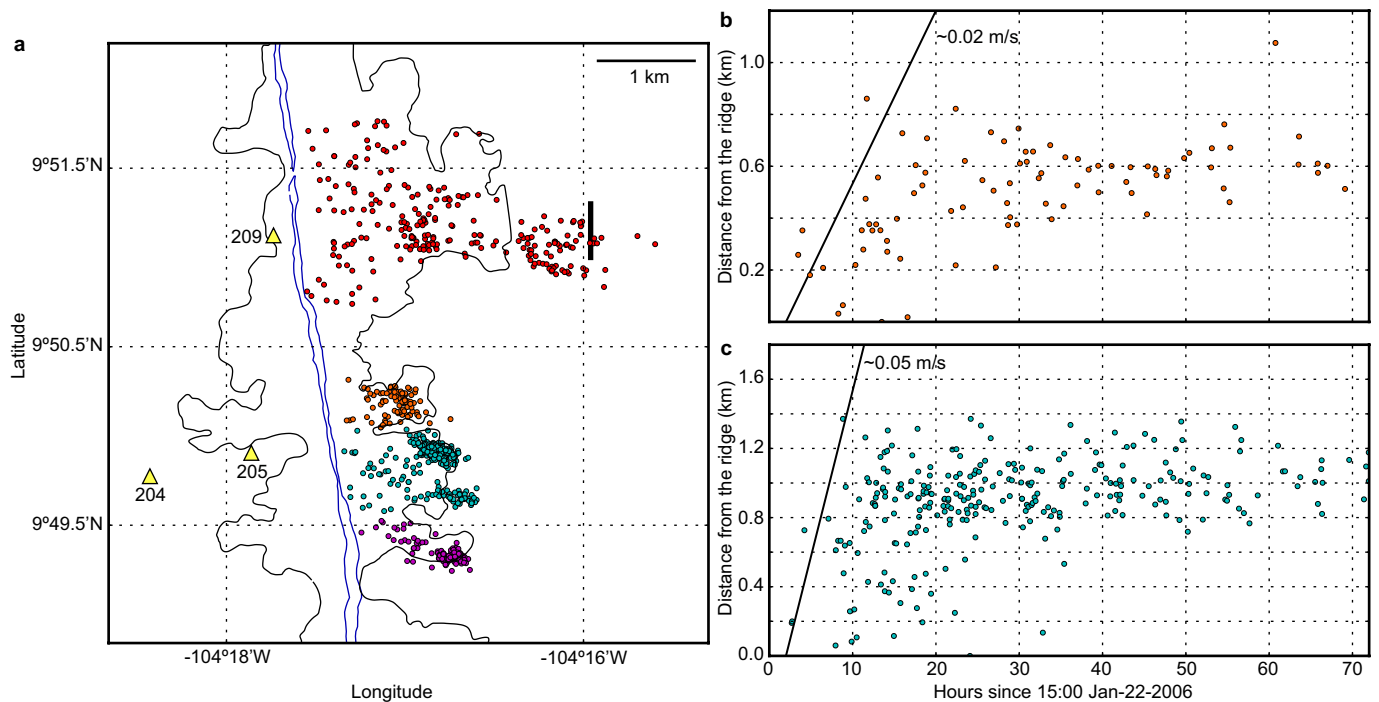
with a width of around 500 m. Earthquakes occurred between 13:30 and 20:00 on 22 January 2006, mostly in the first two hours. The 50 largest-magnitude earthquakes are highlighted with black circles.



Extended Data Figure 4 | Local magnitude of earthquakes.

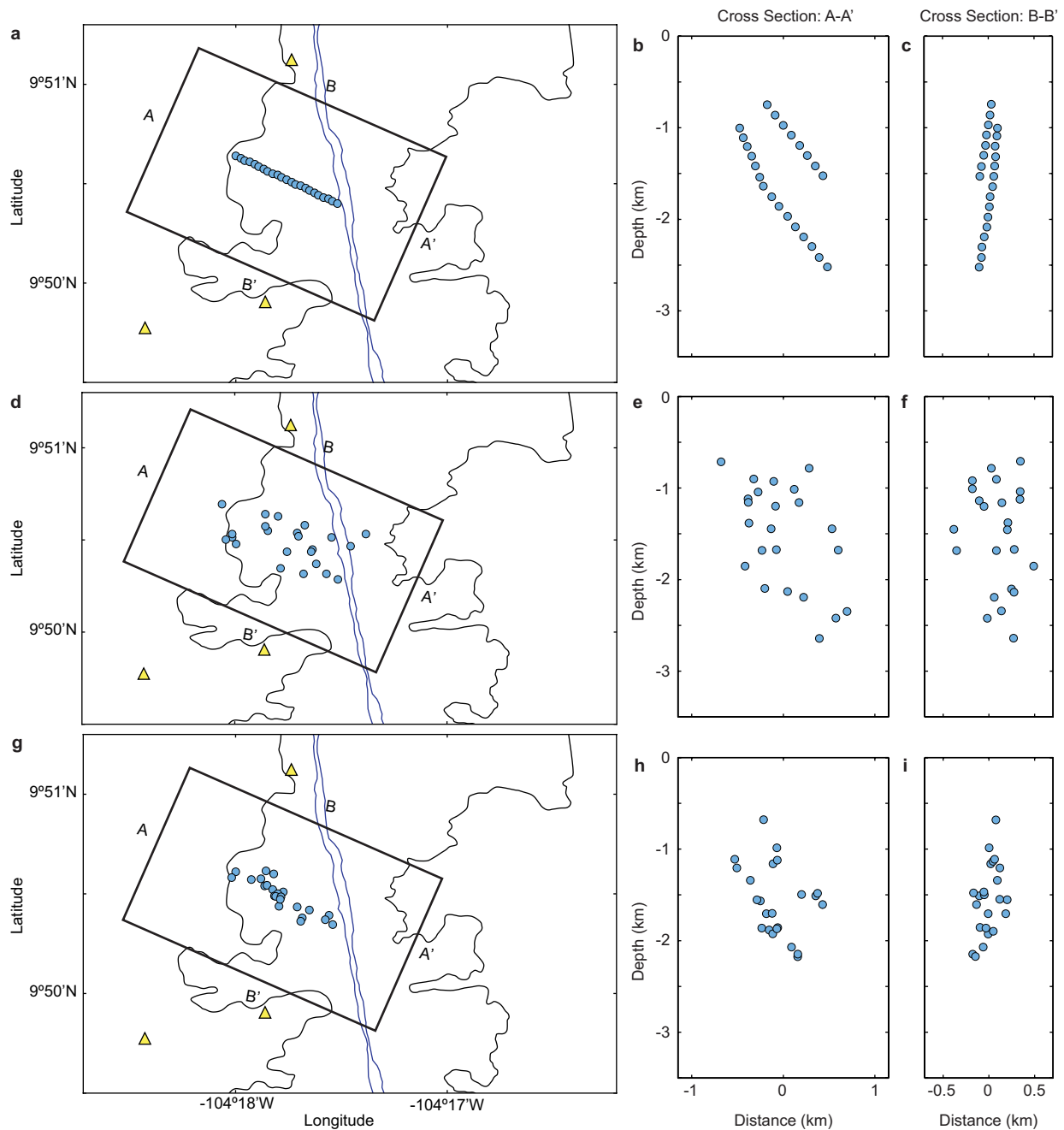
a, Earthquakes show increasing local magnitude M_L with time in a two-hour period leading up to the eruption. Blue dots represent earthquakes during the eruption period analysed in this study in detail while black dots

represent earthquakes over a longer period. **b**, An 8-h zoom-in on panel **a**, demonstrating a clear trend of increasing magnitude immediately before plate rupture.



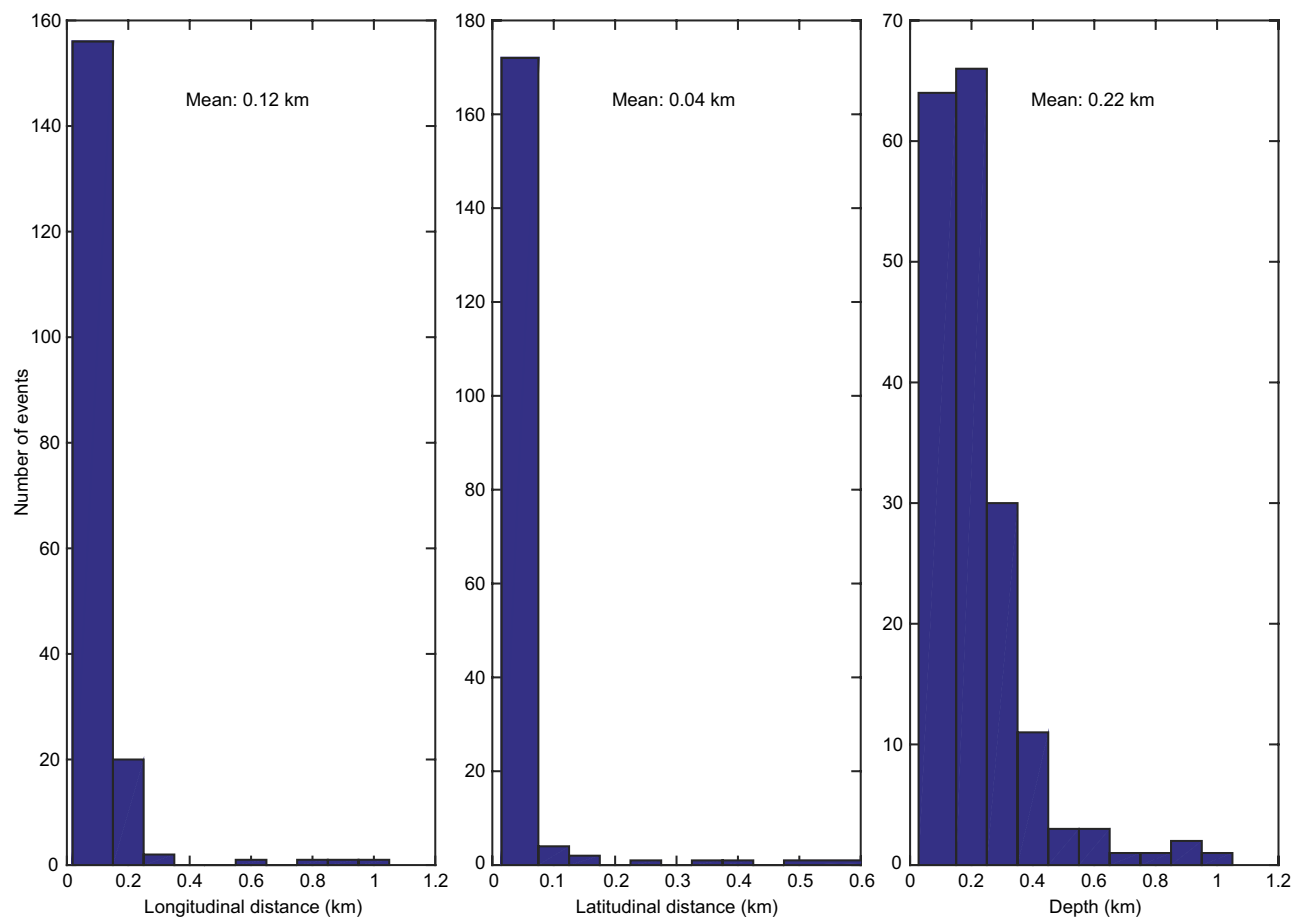
Extended Data Figure 5 | Lava flow velocities. a, Location of seismometers (yellow triangles labelled with station numbers) and impulsive lava events (coloured dots) in the four flow lobes¹⁷ (thin black outline enclosing the lava flow). The bold black line marks the revised

extent of the 2006 lava flow farther off-axis than originally identified¹⁸ (see legend to Fig. 1). b, c, Propagation of impulsive lava events off-axis in two flow lobes.

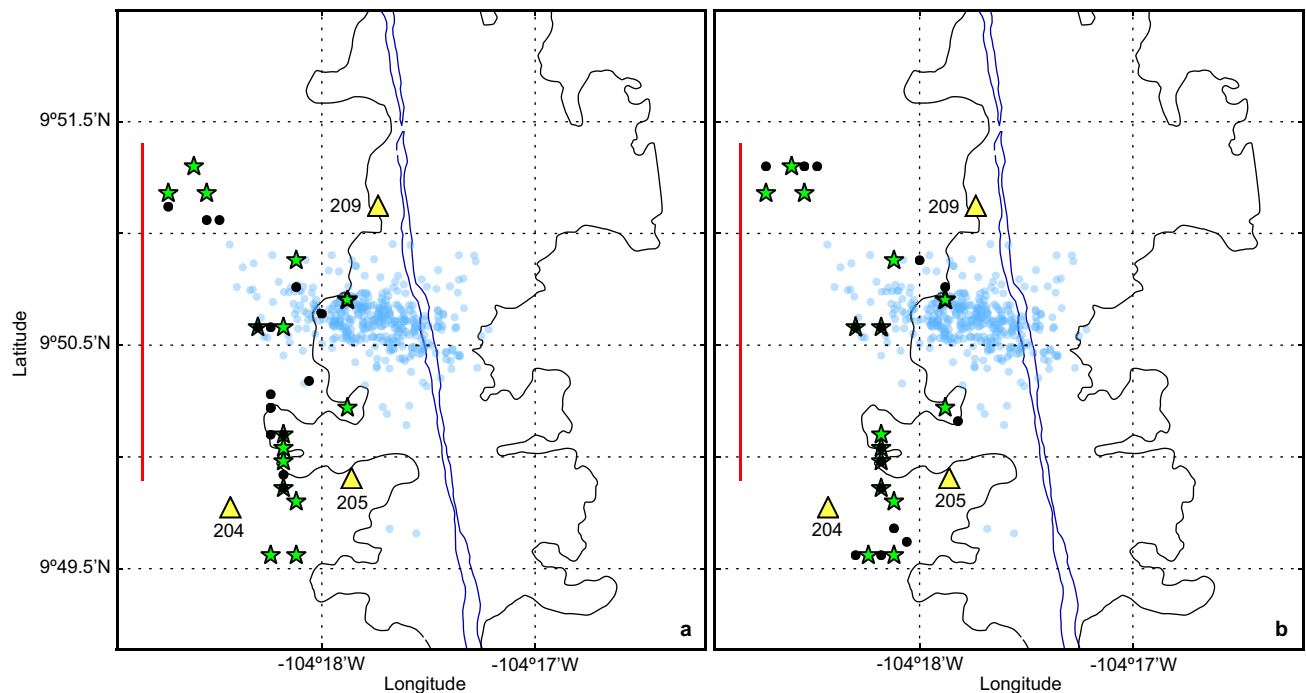


Extended Data Figure 6 | Synthetic test of earthquake locations. **a–c**, Actual locations of synthetic sources. **d–f**, Locations of synthetic sources with normally distributed noise of standard deviation 200 m added. These are used as the initial locations for double difference

relocation. **g–i**, Relocated locations of synthetic sources. Events were relocated using synthetic arrival time with normally distributed noise of standard deviation 0.01 s added.

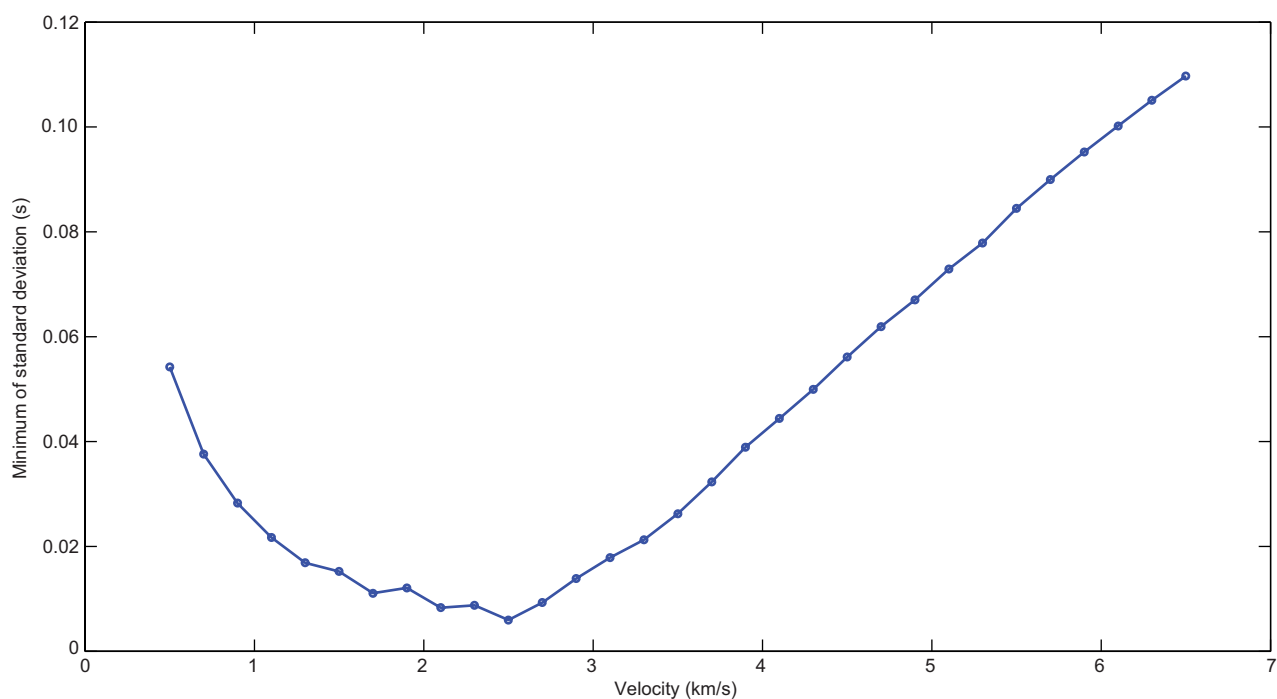


Extended Data Figure 7 | Earthquake relative location errors. Distribution of least-squares errors for the relative locations in longitudinal distance, latitudinal distance and depth.

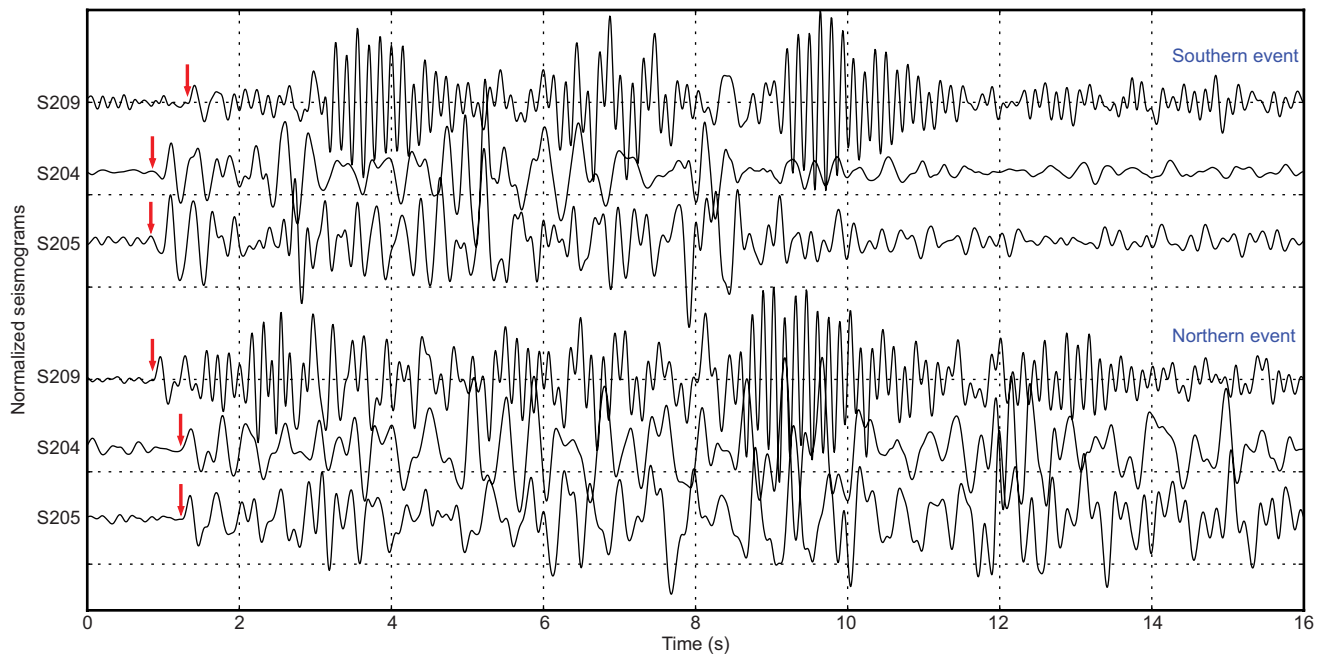


Extended Data Figure 8 | Long-period event locations. **a**, Long-period event locations assuming 0 km depth (black dots) and 1.5 km depth (green stars), assuming a constant crustal velocity of 2.5 km s^{-1} . The red line marks the extent of melt-depleted sub-AML³⁰. Although location depth cannot be definitively determined, the 1.5-h time gap between the initiation of long-period events and melt reaching the surface strongly

supports a deeper source. **b**, Long-period event locations assuming a constant crustal velocity of 2.5 km s^{-1} (green stars) and 2.9 km s^{-1} (black dots) assuming 1.5 km depth. Regardless of the depth and velocity used, events generally cluster near the western edge of the melt lens and bound the area of sub-AML depletion. Faint blue dots represent local earthquake locations (Fig. 1c) for reference.



Extended Data Figure 9 | Long-period event velocity assumption. Minimum of standard deviation for different guess (modelled) velocities, assuming a depth of 1.5 km. The overall minimum of the standard deviation occurs at a velocity of 2.5 km s^{-1} .



Extended Data Figure 10 | Waveforms of long-period events. Waveforms of two separate events at all three stations low-pass filtered at 5 Hz. Red arrows mark the first arrivals. Both event signals arrived at stations S204 and S205 at the same time. This constrains the location of these events

to the west of the ridge axis, between these two stations. The event to the south arrived first at S204 and S205 before S209. The event to the north arrived first at S209 followed by S204 and S205. This constrains the northward migration of the long-period events.